THE JOURNAL OF PHYSICAL CHEMISTRY C
A JOURNAL OF THE AMERICAN CHEMICAL SOCIETY

pubs.acs.org/JPCC
Article

Quasi-Elastic Neutron Scattering of Citrate-Capped Iron Oxide Nanoparticles: Distinguishing between Ligand, Water, and Magnetic Dynamics

Maksim S. Plekhanov, Sabrina L. J. Thomä, Andreas Magerl, Markus Appel, and Mirijam Zobel*

Cite This: J. Phys. Chem. C 2024, 128, 11661−11671
Read Online

ACCESS | Metrics & More | Article Recommendations | Supporting Information

ABSTRACT: Experimental access to the diffusional properties of organic ligand molecules on nanoparticle (NP) surfaces is scarce, although surface functionalization is widespread in synthesis and for the control of functional particle properties. This work focuses on the dynamics of citrate ligands and water molecules on the surface of 6 nm iron oxide NPs (IONPs) equilibrated at a relative humidity of 8% by quasi-elastic neutron scattering. Given the complex quasi-elastic scattering signal including the magnetic nature of the IONPs, we build on fixed window scans to separate multiple dynamic processes, namely, phonons, magnetic relaxations, and hydrogen dynamics. In addition, deuterated samples allowed us to separate the ligand and water dynamics. With a simultaneous fit approach, multiple fixed window scans and energy-resolved spectra are described to determine the activation energies and relaxation times. It is found that surface-bound citrate ligands rotate continuously with E_a = 240 meV and τ_0 = 0.21 ps, while surface water diffuses translationally with E_a = 190 meV and τ_0 = 0.12 ps, significantly slower than bulk water. The separation of the coexisting dynamic processes in this study proves the high potential of quasi-elastic neutron scattering to reach a detailed understanding of interfacial processes in nanostructured materials.

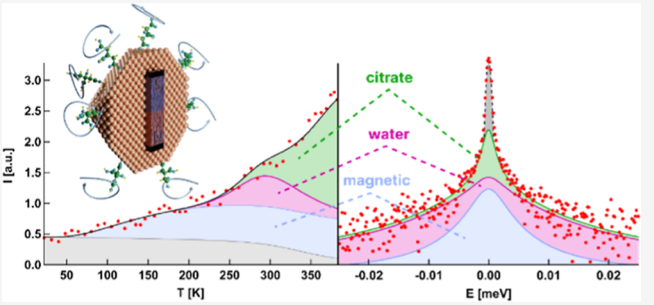

INTRODUCTION

Surface functionalization of nanoparticles (NPs) with organic ligands is pivotal in synthesis and application for controlling their size and shape[1] or stabilizing them in colloidal dispersions.[2] Iron oxide NPs (IONPs) are particularly noteworthy for their extensive use in areas such as magnetic resonance imaging, ferrofluids, and heterogeneous catalysis.[3−5] By functionalizing the IONP surface with biocompatible ligands, their interaction with biological systems can be optimized minimizing toxicity and ensuring compatibility with living organisms.[5] Surface binding of IONPs to spike proteins was shown to play a significant role in COVID-19 treatment.[6]

The dynamics of surface molecules directly influence the stability, reactivity, and functionality of NPs.[7] By investigating the geometry, relaxation times, and activation energies of the motion of the ligands, it is possible to elucidate the mechanisms of ligand binding, detachment, and exchange for controlling the surface chemistry and properties of NPs.[8,9] Experimental techniques used include infrared (IR) spectroscopy addressing the vibrational dynamics of chemical bonds[10] and electron paramagnetic resonance that addresses the motion of spin-labeled ligands and free radicals on an ns scale.[11] Small-angle X-ray and neutron scattering are used to study the ligand−solvent composition within ligand shells.[12] Density functional theory,[13] reverse Monte Carlo,[14] or molecular dynamics simulations complement mechanistic insights into experimental studies, revealing, for instance, that the decanediol surfactant moves closer to the IONP surface and provides better stabilization than sebacic acid.[15] Nuclear magnetic resonance (NMR) is well-suited to investigate the ligands attached to NPs and to distinguish bound and free ligands needed for an understanding of their dynamics and the ligand exchange mechanisms.[16] The time scales probed by NMR span from ms to s with the pulsed field gradient NMR and from ps to ns with relaxation measurements.[17] However, ferromagnetic materials such as IONPs are problematic for NMR investigations due to their interactions with the magnetic field. In contrast, quasi-elastic neutron scattering (QENS) can probe diffusion dynamics for complementary time scales from ∼0.1 ps to 100 ns,[18] in particular for hydrogen-containing (organic) samples with no intrinsic limitation in probing magnetic matter.[19]

Neutrons interacting with matter show, in addition to elastic scattering, energy gain or energy loss scattering. By measuring

Received: January 23, 2024
Revised: May 14, 2024
Accepted: May 23, 2024
Published: June 27, 2024

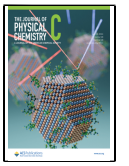

https://doi.org/10.1021/acs.jpcc.4c00479
J. Phys. Chem. C 2024, 128, 11661−11671

Table 1. Ligand Dynamics on the Surface of NPs Investigated by QENS

NPs	ligand	motion type	relaxation time, ps (T of measurement)	activation energy, meV	reference
Fe_xO_y	oleic acid ($C18H_{34}O_2$)	uniaxial rotation	370 (300 K)	34.2	27
	polyisoprene $(C_5H_8)_n$	segmental dynamics[a]	~2 × 103 (300 K)		28
SiO_2	polymethyl acrylate $(C_4H_6O_2)_n$	jump diffusion	50 (420 K)	207	29
PbS	dodecanethiol ($C_{12}H_{26}S$)	uniaxial rotation	220 (300 K)	82.9	25
	hexanedithiol ($C_6H_{14}S_2$)	uniaxial rotation	390 (300 K)	135.0	
Au	hexanethiolate ($C_6H_{13}S$)	uniaxial rotation	2.8 (360 K)	117.1	30
	octadecanethiolate ($C_{18}H_{37}S$)	uniaxial rotation	1.5 (360 K)	273.2	

[a]Nondiffusive relaxations of a group of bonded atoms within a polymer chain.[31].

the distribution of neutrons against the energy transfer $\hbar\omega$, the dynamic structure factor $S(Q,\omega)$ is obtained, where Q is the scattering vector. The dynamic structure factor contains incoherent scattering, describing self-correlation and coherent scattering related to both self- and pair correlation. The large incoherent scattering cross section of hydrogen (σ_{inc}^{H} = 80.27 barns)[20] makes QENS, which measures the near-zero scattering frequency distribution, a particularly attractive technique for studying diffusion dynamics of organic molecules and water by probing the incoherent scattering law $S^{inc}(Q,\omega)$. QENS has tremendously contributed to the understanding of diffusion dynamics of water confined in different environments, such as clays,[21] polymers,[22] and ionic liquids,[23] as well as the formation of hydration water on surfaces of rutile NPs.[24] QENS effectiveness in studying ligand dynamics on the surface of NPs has also recently emerged in a few studies, which have investigated NP systems with bound ligands, featuring comparably strong particle−ligand bonds for which the rotation of the ligand molecule around an axis perpendicular to the NP surface is likely; see Table 1.

The characteristic thermodynamic parameters of a diffusion process's activation energy and relaxation time depend on the type of ligands and NPs. For instance, both dodecanethiol and hexanedithiol grafted onto PbS NPs exhibit rotational diffusion, but the activation energies were found to be 82.9 and 135.0 meV, respectively.[25] In the case of the same ligands but different NPs, it was shown that oleic acid molecules capped onto IONPs undergo localized rotational motion, while oleate ligands were found to diffuse translationally on the surface of PbS NPs.[26,27]

The citrate ligand ($C_6H_5O_7$) is widely employed for improving the stability and biocompatibility of IONPs.[32] Yet, there are few studies investigating the citrate dynamics on the IONP surface, especially in the picosecond−nanosecond time regime. The citrate−IONP system poses several challenges: citrate can be envisaged to diffuse on the surface through the so-called "walking" mechanism—attaching one carboxyl group to the surface, while detaching another, as shown for ZnO NP surfaces.[33] In addition, the magnetic scattering of IONPs complicates the data analysis as magnetic Bragg peaks contribute to the elastic scattering and superparamagnetic relaxations may result in a quasi-elastic signal as shown in refs 34 and 35[34,35] for hematite NPs (Fe_2O_3) with a relaxation time of nanoseconds.

In this study, elastic and inelastic fixed window scans (EFWS and IFWS, respectively) as well as energy-resolved spectra (ERS) together with isotopic labeling were used to separate the contributions of ligands, water, and superparamagnetic relaxations to the quasi-elastic scattering of citrate-capped IONPs and to extract the relaxation characteristics and geometry of the motion of citrate molecules.

METHODS

Sample Synthesis. The synthesis route of the IONPs was established in our previous works.[36,37] A solution of 16 mmol NaOH in 40 g of diethylene glycol (DEG) was added under stirring to the precursor solution containing 2 mmol $FeCl_2 \cdot 4H_2O$ (198.81 g/mol) and 4 mmol $FeCl_3 \cdot 6H_2O$ in 80 g of DEG. Subsequently, the reaction solution was degassed for 2 h in an argon atmosphere and then heated to 220 °C with a ramp of 130 °C/h. For the introduction of the citrate ligands, 2.5 mmol trisodium citrate dihydrate (294.10 g/mol) was dissolved in 1 mL of H_2O and 5 mL of DEG and added between 100 and 120 °C. The synthesis mixture was kept for 1 h at 220 °C and then cooled down to room temperature under further stirring. About twice the volume of acetone was added to precipitate the IONPs. Afterward, the IONP powder was washed with absolute ethanol four times. This IONP powder was then dispersed in water and subsequently freeze-dried.

Sample Characterization: Water and Ligand Content. The content of ligand molecules in the IONP powders was determined with thermogravimetric analysis (TGA) after synthesis as well as prior to and after the neutron experiments (see Table S1). Measurements were carried out in the 30−1000 °C temperature range in argon with a heating ramp of 10 K/min on a Jupiter STA 449 F3 (NETZSCH, Germany). The weight loss attributed to moisture (H_2O) can be determined by analyzing the derivative curve in relation to temperature up to temperatures of ca. 200 °C. The weight loss at higher temperatures is due to the decomposition of the citrate ligand molecules. The remaining mass of the sample is the IONPs (see Figure S1). The TGA results were confirmed by elemental analysis of carbon, hydrogen, and nitrogen (CHN), performed on 1.98−2.43 mg of the nanocrystalline powder with an Elementar vario EL III instrument (Elementar, Germany). The results of the TGA and CHN are in good agreement as shown in Table S1. All TGA and CHN measurements were carried out without equilibrating samples at a specific relative humidity (RH) as the main purpose was to determine the amounts of ligand in the sample. The water content determined from the TGA was used as a starting point for the estimation of water in the sample after equilibration with fine balance measurements.

Sample equilibration at 8% RH was done by placing the sample in an open container for the neutron scattering experiment into a desiccator with oversaturated sodium hydroxide solution in either H_2O or D_2O and a hydrometer for monitoring RH. The sample was kept for at least 48 h and was considered equilibrated when the weight stopped changing over time as controlled with a fine balance. Before the QENS experiment, the containers were taken out of the desiccators and closed within a few minutes with their lids using indium seals, and the mass change between before and after

https://doi.org/10.1021/acs.jpcc.4c00479
J. Phys. Chem. C 2024, 128, 11661−11671

equilibration was determined with a fine balance. The resulting mass loss can be found in Table S2.

The sample thickness of 1 mm was used in order to achieve a neutron transmission of 90% and reduce the multiple scattering probability.

Small-angle X-ray scattering (SAXS) patterns were recorded with the laboratory SAXS system "Ganesha-Air" from SAXSLAB, Xenocs. The X-ray source is a D2-MetalJet (Excillum) operating at 70 kV and 3.57 mA with Ga Kα radiation (λ = 0.1341 nm) providing a brilliant and small beam (<100 μm). Measurements were done in 2.1 mm borosilicate glass capillaries (Hilgenberg, code 1409364, Germany) at room temperature, and the diffracted intensity was recorded by a position-sensitive detector (PILATUS 300 K, Dectris). To cover the range of scattering vectors between 0.065 and 5.425 nm^{-1}, different detector positions were used.

QENS and Neutron Powder Diffraction Measurements. QENS experiments on the hydrated samples were performed at the backscattering spectrometer (BS) IN16B at the Institut Laue-Langevin (ILL, Grenoble, France) with a wavelength of 6.271 Å, an energy resolution of half-width half-maximum (HWHM) ≈ 0.37 μeV, and an energy range of ±30 μeV.[38,39] Additional QENS measurements in Backscattering and Time-of-Flight Spectrometer (BATS, IN16B)[40] mode were performed with an energy resolution of HWHM ≈ 1.9 μeV and an energy range from −142 to +186 μeV.[41] The ERS were collected at 340, 360, and 380 K. FWSs were taken in the temperature range of 2−380 K on the elastic line (EFWS) and at an energy offset of 3 μeV (IFWS). Both FWS and ERS were measured over a Q range of 0.19−1.79 Å^{-1} divided into 17 detector banks, see Table S4 for details. FWS and ERS were measured for 9 and 4 h, respectively. The data reduction was performed with the software package Mantid[42] according to standard procedures for IN16B. The IONP sample measured at 2 K was used as the instrumental resolution for the data evaluation.

QENS measurements on the D_2O-equilibrated sample were carried out at 370 K at the BS EMU at the Australian Nuclear Science and Technology Organisation (ANSTO, Australia), which has characteristics similar to those of IN16B, albeit with a reduced neutron flux. The Q range covers 0.35−1.95 Å^{-1} with a step of 0.1 Å^{-1}. A vanadium sample was used for normalization purposes and to define the resolution function. The experimentally determined shape of the resolution was convolved with the model functions during the fit of all ERS measurements.

NPD data of a D_2O-equilibrated sample equilibrated at 8% RH were taken at room temperature on the instrument WOMBAT at ANSTO using a wavelength of 2.41 Å.[43] For Rietveld refinement the software package, GSAS II was used.[44,45]

QENS Data Analysis. A simultaneous fit approach was utilized to fit ERS, EFWS, and IFWS data sets. Three processes of low-temperature magnetic relaxation, water diffusion, and citrate motion were described with corresponding activation energies E_a and relaxation times τ_0 according to eqs 2−13. The details can be found in Supporting Information Section IV. b.

RESULTS AND DISCUSSION

Sample Characterization. The obtained IONPs are 6.4 ± 0.6 nm in diameter, according to Rietveld refinement (see Figure S2), and 5.8 ± 0.9 according to SAXS measurements (see Figure S3). This is in good agreement with the results of our previous work.[46] The IONPs can crystallize as the magnetite phase with the space group $Fd\bar{3}m$[47] as well as maghemite described with the $P4_3$ 31 space group or, in case of cation vacancy ordering, with lower-symmetry space groups $P4_3\,2_1\,2$ or $P4_1\,2_1\,1$.[48] As shown in Figure S2, the NPD pattern of the sample can be described with the mixture of maghemite and magnetite phases. In the Q range of the BS instrument, the main Bragg peak located at $Q \sim 1.31$ Å^{-1} is mainly of magnetic origin.

The content of ligand molecules in the IONP powders was determined with TGA before and after neutron experiments (Table S1). The weight loss attributed to moisture (H_2O) can be determined from the TGA curve up to a temperature of ca. 200 °C. The weight loss at higher temperatures is due to the decomposition of the citrate ligand molecules. During the synthesis, excess of sodium hydroxide was used, thus creating a basic pH of the solution, which should result in completely deprotonated carboxyl groups, as the pK_{a3} of citric acid is 6.4.[49] By taking into account the scattering cross sections of each atom[20] and the composition of the sample, the coherent and incoherent contributions to the scattering signal can be estimated (see Table S3). The incoherent contributions of citrate and water are 61.4 and 37.9%, respectively. Hence, water contributes significantly to the scattering signal.

As was shown in previous works, the IONPs are truncated octahedrons with hexagonal facets featuring a particle radius of around 3 nm.[37] The diagonal of a hexagonal facet is approximately 4 nm, with a ligand coverage of 2.8 ligand/nm^2. Depending on how many iron surface sites are blocked by a single citrate molecule, this corresponds to 0.5−1.3 layers of surface coverage.[46] According to Bixner et al.,[50] there are 3.5−5.9 iron sites/nm^2 in magnetite, thus there is enough iron oxide surface for interactions with both ligand and water molecules. Previous inelastic and quasi-elastic studies on IONPs as well as Mössbauer spectroscopy have identified superparamagnetic relaxations that occur below 100 K.[35,51] The relaxation nature of spin flips is described by the Néel−Brown law.[52] The superparamagnetic behavior of IONPs was also demonstrated with field-dependent magnetometry in our previous work.[36]

FWSs in Magnetic and Nonmagnetic Regions. Concluding from the characterization of the sample, contributions to the QENS signal from citrate, water, and superparamagnetic relaxations can be expected. The geometry of the ligand motion would likely depend on the surface-binding mechanism. There are studies suggesting a mixture of mono- and bidentate binding.[53−55] Previous IR spectroscopy measurements on citrate-capped IONPs showed higher relevance of monodentate binding. However, due to broad absorption peaks, a complete separation of binding modes could not be made.[36] Firmly capped ligands would likely move rotationally, appearing as a localized motion in the QENS signal. In the case of both mono- and bidentate binding mechanisms, rotational motion of functional groups is possible. If tridentate binding is present, these molecules would likely be rendered immobile. In the case of the dynamically changing binding, ligands could employ a walking mechanism suggested for citrate on ZnO NPs[33] or detach from the surface and diffuse translationally. For the motion of water molecules, both rotational and translational modes could be expected, with relative contributions depending on such parameters as water content or strength of the interaction between the water molecules and NP surface.[56]

https://doi.org/10.1021/acs.jpcc.4c00479
J. Phys. Chem. C 2024, 128, 11661−11671

FWS measurements were performed over a Q range of 0.19−1.79 Å^{-1} to obtain a quick overview of the dynamics in a wide temperature range of 2−380 K. These experiments involve measuring the neutron intensity at a specified energy transfer, in contrast to ERS, which are measured at a specific temperature over all available energies. Both FWS and ERS measurements were performed at BS IN16B with a wavelength of 6.271 Å, an energy resolution of HWHM ≈ 0.37 μeV, and an energy range of ±30 μeV on IONPs equilibrated in 8% RH. In order to access shorter relaxation times, additional ERS measurements were done in BATS mode at IN16B with an energy range from −142 to +186 μeV.

In the NPD pattern shown in Figure 1, the main Bragg peak occurs at Q = 1.31 Å^{-1}, which is present in both magnetite and

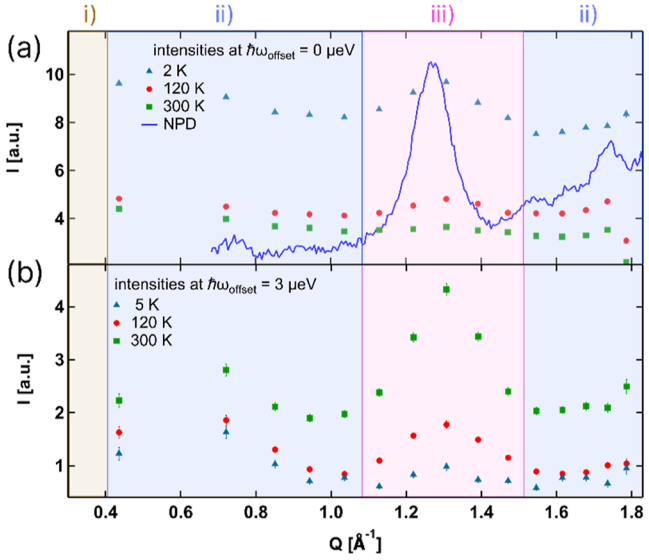

Figure 1. (a) Intensity at 2, 120, and 300 K from the EFWS, plotted along with the NPD pattern of IONPs measured at RT; (b) intensity at the energy offset of 3 μeV and temperatures of 5, 120, and 300 K.

maghemite phases.[57] Two less pronounced Bragg peaks at Q = 1.53 and 1.74 Å^{-1} indicate the presence of the maghemite phase.[57,58]

The NPD data has better resolution in Q than elastic intensities obtained from a BS and, the peaks in EFWS intensities are significantly broader (for the full NPD pattern see Figure S2). The low Q range <0.43 Å^{-1} is affected by small-angle scattering (see Figure S3).[59] We note that the small-angle contribution does not end abruptly at a specific detector; thus, the chosen boundaries of the small-angle range include the detectors that show a very pronounced influence of small-angle scattering. Therefore, within the BS Q range, we assign three regions located in four Q ranges:

i Q < 0.43 Å^{-1} (Q0−Q2)—affected by small-angle scattering;
ii 0.43 < Q < 1.12 Å^{-1} (Q3−Q6) and 1.47 < Q < 1.79 Å^{-1} (Q12−Q16)—scattering mostly from nuclei in the sample; hereinafter referred to as the non-Bragg region;
iii 1.12 < Q < 1.47 Å^{-1} (Q7−Q11) main magnetic Bragg peak; hereinafter referred to as the Bragg region.

The resolution function, centered at 0 μeV, has a Lorentzian-like decay. This causes some intensity even for an offset of 3 μeV in regions where there is strong elastic intensity like in the Bragg range around Q = 1.31 Å^{-1}, as well visible in Figure 1b. The magnetic origin of the Bragg peak (see Figure S2) and the fact that the peak in Figure 1b becomes more pronounced with increasing temperatures (120 and 300 K) imply magnetism-related relaxations in this Q range. Hence, for the investigation of the dynamics of hydrogen-containing species on the surface, the non-Bragg Q regions (ii) 0.43 < Q < 1.12 Å^{-1} and 1.47 < Q < 1.74 Å^{-1} are the most interesting,

Figure 2 shows fits of the FWS in a non-Bragg region at a Q value of 1.62 Å^{-1}, as well as in the Bragg region at Q = 1.31 Å^{-1}. The intensity I_{EFWS} contains static diffuse scattering arising from lattice defects, incoherent scattering from the IONPs, the signal from dynamics too slow for the energy resolution, the elastic incoherent structure factor [EISF or $A_0(Q)$] of local motions, and the amplitudes of Lorentzian profiles for an energy transfer = 0. One of the reasons for the decrease of the elastic scattering is thermal vibrations. This is usually accounted for by the Debye−Waller factor (DWF), with a mean square displacement (MSD or $\langle u^2 \rangle$).

$$\mathrm{DWF} = \exp\left(-\frac{1}{3}Q^2\langle u^2\rangle\right) \tag{1}$$

For temperatures above the Debye temperature θ_D, when the entire phonon spectrum is thermally excited, the MSD increases linearly with temperature. However, below θ_D, the phonon density of states (DOS) must be taken into account. More detailed expression of $\langle u^2 \rangle$ with the consideration of DOS can be found in the Supporting Information, Section III.

For each Q value, the intensities in the EFWS and IFWS were fitted as a function of temperature with eqs 2 and 3 according to Grapengeter et al.[60]

$$I_{EFWS}(Q, T) = \mathrm{DWF}(Q) + \left(bkg_{EFWS}(Q) + \sum_i^n A_0(Q)_i + \frac{2}{\pi}(1 - A_0(Q)_i)\arctan\left(\frac{\tau(Q)_i}{\tau_{res}}\right)\right) \tag{2}$$

with $A_0(Q)_i$ being the EISF of the ith dynamic process, τ_{res} is the instrumental resolution, n is the number of processes, and DWF is obtained according to eq 1. The background $bkg_{IFWS}(Q)$ contains all of the remaining elastic intensity, including the incoherent and diffuse scattering from the IONPs.

The IFWS intensity is given by

$$I_{IFWS}(Q, T) = \mathrm{DWF}\left(bkg_{IFWS}(Q) + \sum_i^n B(Q)_i \cdot \left(\frac{\tau(Q)_i}{1 + \omega_{off}^2\tau(Q)_i^2}\right)\right) \tag{3}$$

where $bkg_{IFWS}(Q)$ is the background contribution from the wings of the resolution function, which is described here with the shape of the EFWS, scaled accordingly at the corresponding Q value. Furthermore, B_i is the scaling parameter, ω_{off} is the energy offset of the IFWS in units of frequency, and $\tau(Q)_i$ is the relaxation time of the ith dynamic process, expressed as

$$\tau(Q)_i = \tau_0(Q)_i \exp\left(\frac{E_{a_i}}{k_B T}\right) \tag{4}$$

https://doi.org/10.1021/acs.jpcc.4c00479
J. Phys. Chem. C 2024, 128, 11661−11671

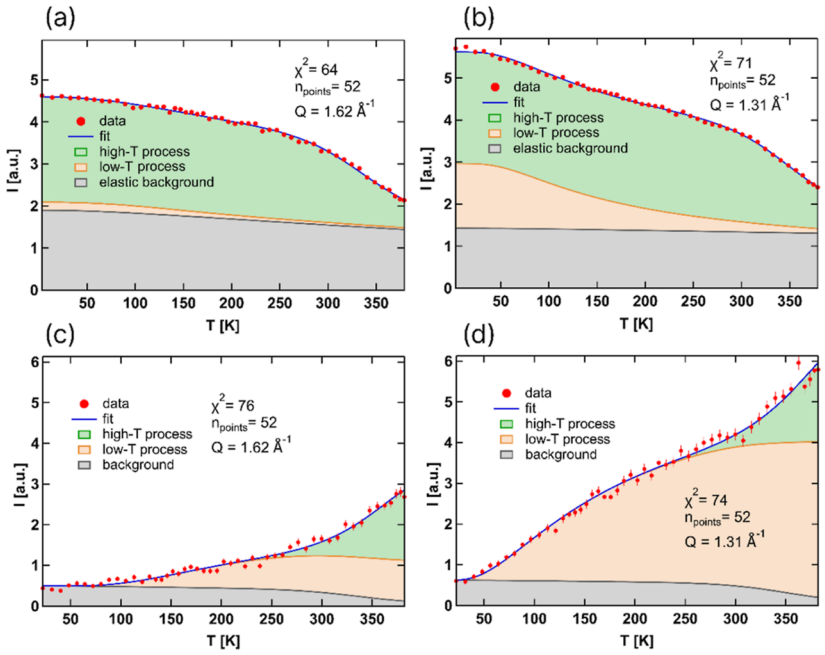

Figure 2. Fits of the EFWS (a,b) and IFWS at 3 μeV energy offset (c,d) at $Q = 1.62$ Å^{-1} (a,c) and $Q = 1.31$ Å^{-1} (b,d). At each Q value, the EFWS and IFWS are fitted simultaneously, according to eqs 2 and 3 with shared $\tau(Q)$ for each process.

with E_{ai} as the activation energy of the ith dynamic process and $\tau_0(Q)_i$ as the high-temperature relaxation time limit of the ith dynamic process. $\tau(Q)$ is related to the HWHM Γ of a Lorentzian function commonly employed to model QENS broadening

$$\Gamma(Q) = \hbar\frac{1}{\tau(Q)} \tag{5}$$

The equations above rely on the assumption that the described dynamic processes follow the Arrhenius law, which is not always the case. They also assume independent motion, which otherwise would require a convolution of two processes if they influence one another. The resolution is accounted for only in terms of its width, and in the case of the IFWS can still contribute to the background and influence the scaling parameter B in eq 3. Therefore, initial information can be obtained from the FWS only, yet these assumptions need to be taken into account.

The IFWS and EFWS are fitted simultaneously using eqs 2 and 3, with relaxation times and activation energies shared between the data sets. Both types of FWSs are well-described with two dynamic contributions (Figure 2). At the Bragg peak (Figure 2b,d), however, the amplitude of the low-temperature contribution is significantly increased, implying the different natures of the processes.

From the FWS fits in the non-Bragg region, the E_a for the low-temperature process of 20.8 ± 2.8 meV was obtained. This agrees well with previously reported values for superparamagnetic relaxations of mesoporous iron oxide of 19.8 meV.[51] The activation energy of magnetic relaxations at the Bragg peak of 17.8 ± 2.1 meV is also within the margin of error of the previously reported E_a of superparamagnetic relaxations. Thus, the low-temperature process is assigned to the magnetic relaxations.

Up to this point, from the FWS, we identify:

1 a low-temperature magnetic process for all Q values;[27,28]
2 this magnetic process is either amplified or accompanied in the magnetic Bragg region by a second low-temperature contribution;
3 a high-temperature process well visible across all Q values at temperatures above 200 K. This process is likely related to the motion of hydrogen atoms belonging to ligands and/or water.

The IONPs were equilibrated in 8% RH, which removed a significant amount of water from the powder, as shown by fine balance measurements in Table S2. About 2.5 wt % of water remained in the sample compared to 17 wt % of citrate molecules, as determined by TGA and CHN analysis (see Tables S1−S2). The samples feature no surface hydroxyl groups.[46] Since the QENS signal arises dominantly from the incoherent scattering of hydrogen, the molar ratio of H in citrate and water molecules is the critical factor. As shown in Table S3, about 38% of incoherent scattering stems from water; a significant contribution to a QENS signal from water dynamics is expected. Thus, a scattering law with at least three dynamic processes, corresponding to the ligand, water, and magnetic dynamics, should be used to describe the data. However, FWS measurements alone are not sufficient to distinguish water and citrate motion, as a function with two processes describes well both FWSs and including a third process does not improve the fit. In order to resolve the citrate and water dynamics, we proceed to ERS modeling.

ERS Distinguishing Citrate and Water Motion. Based on FWS analysis and the sample composition, the contributions to the scattering law can be written as

$$S^{\mathrm{cit}}(Q,\omega) = A_0^{\mathrm{cit}}(Q)\delta(Q) + (1 - A_0^{\mathrm{cit}}(Q))L^{\mathrm{cit}}(Q) \tag{6}$$

$$S^{\mathrm{water}}(Q,\omega) = A_0^{\mathrm{water}}(Q)\delta(Q) + (1 - A_0^{\mathrm{water}}(Q))\, L^{\mathrm{water}}(Q) \tag{7}$$

$$S^{\mathrm{mag}}(Q,\omega) = A_0^{\mathrm{mag}}(Q)\delta(Q) + (1 - A_0^{\mathrm{mag}}(Q))L^{\mathrm{mag}}(Q) \tag{8}$$

https://doi.org/10.1021/acs.jpcc.4c00479
J. Phys. Chem. C 2024, 128, 11661−11671

Where $S^{cit}(Q,\omega)$, $S^{water}(Q,\omega)$, and $S^{mag}(Q,\omega)$ are the contributions from the citrate, water, and magnetic dynamics, respectively, A_0^i is the EISF of the corresponding dynamic process, and L^i is a Lorentzian function defined as

$$L^i \equiv \frac{1}{\pi} \times \frac{\Gamma(Q)_i}{(\hbar\omega)^2 + \Gamma(Q)_i^2} \tag{9}$$

with $\hbar\omega$ being the energy transfer and $\Gamma(Q)_i$ denoting the HWHMs of the ith Lorentzian curve, related to its relaxation time and activation energy through eqs 3 and 4.

The measured intensity can be written as

$$I^{exp}(Q,\omega) = n^{exp}\mathrm{DWF}(Q)[n^{el}\delta(Q) + n^{cit}S^{cit}(Q,\omega) + n^{water}S^{water}(Q,\omega) + n^{mag}S^{mag}(Q,\omega)] \otimes R(Q,\omega) \tag{10}$$

where n^{exp} is a common experimental scaling factor, DWF is the Debye−Waller factor for the whole system, n^{el} is the scaling factor of all remaining elastic scattering, n^{cit} and n^{water} are coefficients proportional to hydrogen scattering cross section and the number of hydrogens from the ligand and water molecules, respectively, n^{mag} is the scaling factor proportional to the number of atoms, contributing to the magnetic process and its Q-dependent magnetic scattering cross section, and $R(Q,\omega)$ is the instrumental resolution function. The full equation combining eqs 5−10 can be found in Supporting Information Section IV.

For the fitting, the combination of eqs 5−9 was condensed to

$$S^{fit}(Q,\omega) = \mathrm{DWF}(Q)[A_{eff}^0(Q)\delta(Q) + A_{eff}^{cit}(Q)L^{cit}(Q) + A_{eff}^{water}(Q)L^{water}(Q) + A_{eff}^{mag}(Q)L^{mag}(Q)] \otimes R(Q,\omega) \tag{11}$$

The absolute values of the multiplied coefficients $n^{exp}n^i$ in eq 10 are unknown. Therefore, all of the EISFs multiplied by their scaling factor are fitted together as an effective elastic intensity amplitude A_{eff}^0. The amplitudes for each Lorentzian for the ith dynamic process are defined as

$$A_{eff}^i(Q) = p\cdot n^{exp}\cdot n^i\cdot \mathrm{ISF}^i(Q) \tag{12}$$

where p is a fraction of mobile species observable with the instrumental resolution and ISF^i is the incoherent structure factor of the ith dynamic process defined as

$$\mathrm{ISF}^i(Q) = 1 - A_0^i(Q) \tag{13}$$

To distinguish the contribution of diffusive processes of citrate and water molecules to the QENS signal, ERS measurements of the H_2O- and D_2O-equilibrated samples were carried out. A negligible exchange of citrate ^1H atoms is assumed.

Figure 3 shows the ERS measured at 360 K in BATS mode at IN16B and at 370 K on the BS instrument Emu on the H_2O- and D_2O-equilibrated samples, respectively. The spectra obtained in the BATS mode have broader energy transfer and resolution ($\Delta E^{BATS} = \pm 150$ μeV; resolution function $\mathrm{HWHM}_{resol}^{BATS} \sim 1.9$ μeV) compared to the BS mode ($\Delta E^{BS} = \pm 31$ μeV; resolution function $\mathrm{HWHM}_{resol}^{BS} \sim 0.5$ μeV). Two Lorentzians denoted as L^{water} and L^{mag} are present in the BATS data with respective HWHMs of 0.039 ± 0.003 and 0.004 ± 0.002 meV at $Q = 1.62$ Å^{-1}. In the narrower energy transfer of

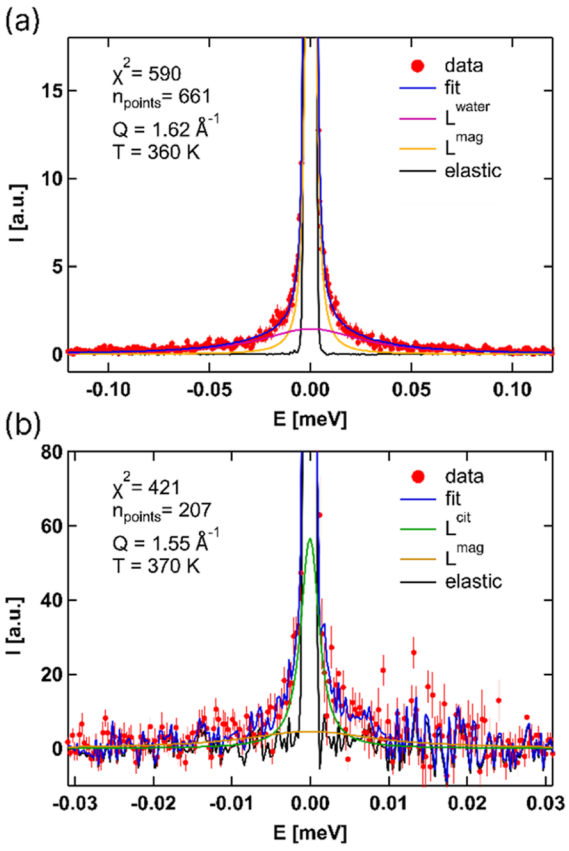

Figure 3. ERS measured at 360 K at IN16B in BATS mode for an H_2O-equilibrated (a) and at 370 K on the BS Emu for a D_2O-equilibrated sample (b).

a BS spectrum of the D_2O-equilibrated sample, two Lorentzians denoted as L^{cit} and L^{mag} have HWHMs of 0.001 ± 0.004 and 0.011 ± 0.008 meV, respectively, therefore the HWHMs of L^{mag} are the same for BS and BATS measurements within the margin of error. The L^{cit} Lorentzian is not shown in the BATS data, as it is too narrow to be properly resolved, yet a small contribution from the wings of the citrate Lorentzian is possible. The L^{water} Lorentzian should be visible in the BS data, but since for this BS measurement, the sample is equilibrated in D_2O, L^{water} is not observed. A more detailed investigation of water motion is described below with the simultaneous fit approach.

Unifying Picture of Dynamics by Simultaneous Fit of the FWS and ERS. To extract meaningful parameters of the dynamic processes, a simultaneous fit routine was used describing together two FWSs with energy offsets of 0 and 3 μeV as well as two ERS at 340 and 380 K measured on the BS at IN16B on the H_2O-equilibrated sample. During these simultaneous fits, χ^2 values for all data sets were minimized together. Hereby, τ_0 and E_a (see eqs 2−5) were used as common global parameters for the HWHM of the Lorentzians. The ratios of the intensities of the Lorentzians were coupled in between data sets, too. The fit was applied to the Q values outside of the small-angle and Bragg peak regions. The model with three processes was used as prompted by the insights from FWS fittings and ERS measurements of the D_2O-equilibrated sample. A simultaneous fit with a two-process model was attempted as well, as was done in the FWS section. However, the fit with the two-process model was not adequate. Additionally, the model is supported by comparing the total

https://doi.org/10.1021/acs.jpcc.4c00479
J. Phys. Chem. C 2024, 128, 11661−11671

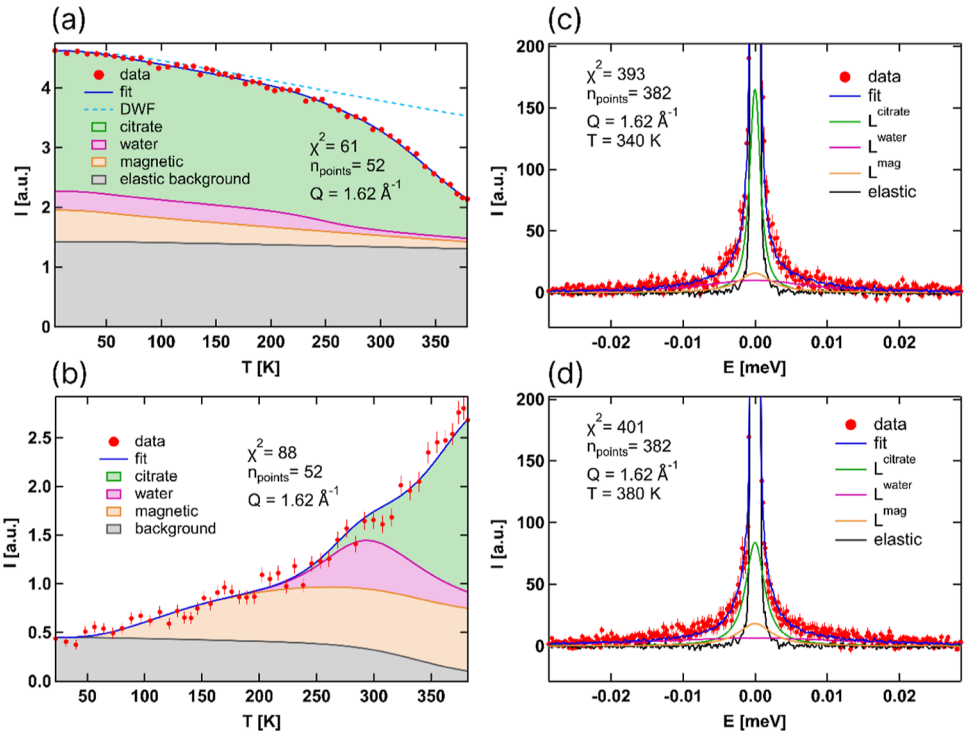

Figure 4. Simultaneous fit of the EFWS (a), IFWS (b), and ERS at 340 (c) and 380 K (d).

integrated intensities with the DWF, calculated from fitted Debye temperatures. As can be seen in Figure S6, the DWF and total intensity match quite well outside of the Bragg region. In the Bragg region, however, the model with three quasi-elastic processes is not sufficient.

The simultaneous fit of several data sets increases the stability of the fit, allowing the application of more complex models. Thus, the citrate, water, and magnetic dynamics could be disentangled without fixing any parameters. Similar results were demonstrated by Mamontov et al.[61] applying a global fit approach to multiple ERS at different Q values. More details on the simultaneous fit implementation can be found in the Methods section.

The results of the simultaneous fit for Q = 1.62 Å^{-1} are shown in Figure 4 and the values of the fitted parameters are contained in Table 2. The fits of the ERS at 340 K in and outside of the Bragg region are shown over the full energy and intensity range in Figure S4. It is evident that the simultaneous fit with three dynamic processes allows for a good description of the data outside of the Bragg peak.

The E_a and τ_0 of the citrate motion do not show a Q^2 independence (see Figure 5a), yielding a constant HWHM of the Lorentzian describing the citrate motion (L^{cit}) and implying the absence of translational diffusion. Similar behavior has been obtained from the individual fits of the ERS measurements of the D_2O-equilibrated sample (see Figure 3), which confirms that L^{cit} represents the citrate motion. The absence of translational diffusion of the ligands implies that they are firmly grafted on the surface. The suggestion of citrate ligands being strongly bonded to the surface is also supported by IR studies, which demonstrate that citrate ligands exhibit a mixture of mono- and bidentate binding.[53,54] The bidentate binding restricts the rotational motion, rendering these ligands less mobile. The E_a of 239 ± 12 meV of the citrate motion is higher than those for most of the other ligand−NP systems,

Table 2. Values of Fitted Parameters as Introduced in Eqs 5−11 Obtained from the Simultaneous Fit for Q = 1.62 Å^{-1} and Calculated HWHMs of Each Lorentzian

fit parameter	value (340 K)	value (380 K)
A_{eff}^{0}, [a.u.]	0.64 ± 0.06	0.56 ± 0.05
A_{eff}^{cit}, [a.u.]	0.61 ± 0.20	0.59 ± 0.23
τ_0^{cit}, [ps]	0.21 ± 0.40	0.21 ± 0.40
Ea^{cit}, [meV]	239 ± 12	239 ± 12
$\Gamma_{calc}{}^{cit}$, [meV]	0.001 ± 0.004	0.002 ± 0.009
A_{eff}^{water}, [a.u.]	0.19 ± 0.13	0.23 ± 0.10
$\tau 0^{water}$, [ps]	0.12 ± 0.27	0.12 ± 0.27
E_a^{water}, [meV]	189 ± 7	189 ± 7
Γ_{calc}water, [meV]	0.009 ± 0.019	0.017 ± 0.039
A_{eff}^{mag}, [a.u.]	0.21 ± 0.13	0.22 ± 0.17
τ_0^{mag}, [ps]	50.46 ± 23.48	50.46 ± 23.48
E_a^{mag}, [meV]	34 ± 2	34 ± 2
$\Gamma_{calc}{}^{mag}$, [meV]	0.004 ± 0.002	0.005 ± 0.002
θD, [K]	382.18 ± 0.07	0.07

summarized in Table 1. This could be explained by the fact that in bigger ligand molecules, such as oleic acid, the motion is segmental, and different parts of the ligand chain may start to rotate at different temperatures.[27] The citrate ligand is small and does not have many degrees of freedom of motion. Therefore, the dynamics described here likely correspond to the whole ligand molecule and not to its parts, requiring higher activation energies.

The Lorentzian describing water motion exhibits a Q^2 dependence, see Figure 5c. The low Q range of the dependence can be fitted with Fick's law of diffusion: $\Gamma = \hbar DQ^2$. This results in a water diffusion coefficient $D^{360\ K} = 9 \times 10^{-11}$ m^2/s, which is lower than the bulk water diffusion coefficient at 363 K of $D_{bulk}^{363\ K} = 981 \times 10^{-11}$ m^2/s.[62] This is consistent since the diffusion of residual water molecules on the surface is likely constrained by the citrate ligands compared

https://doi.org/10.1021/acs.jpcc.4c00479
J. Phys. Chem. C 2024, 128, 11661−11671

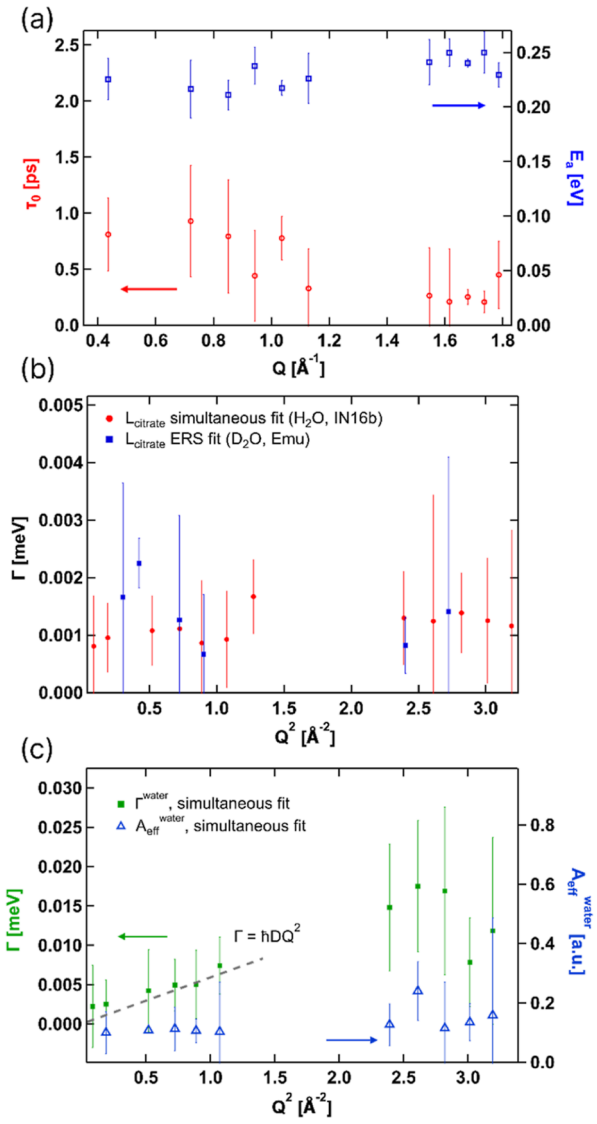

Figure 5. (a) Activation energy and relaxation time limit of citrate motion; (b) HWHM of citrate Lorentzian from H_2O- and D_2O-equilibrated samples (370 K); (c) HWHM and the amplitude of water Lorentzian from simultaneous fit (360 K).

to the bulk water. The translational diffusion observation is also consistent with the Q-independent amplitudes of the water Lorentzian, shown in Figure 5c. Even though the HWHMs of water and citrate Lorentzians are similar, especially toward lower Q values, their amplitudes differ significantly (Figures 5c and 6). Additionally, by employing a simultaneous fit approach, each Lorentzian is described in the whole temperature range through the Arrhenius law. These two facts allow for clearer separation of the processes, even if for a specific Q value and temperature, they could be difficult to distinguish.

To study the geometry of the ligand rotation, the Q dependence of the corresponding ISF is shown in Figure 6 (see eqs 11−13). The value of $A_{\mathrm{eff}}^{\mathrm{cit}}$ is decreasing toward zero at low Q, while it approaches a constant value at higher Q values. This is characteristic of localized motion.[63] A powder-averaged rotational model of continuous diffusion on a circle of a radius r was fitted to the Q dependence of $A_{\mathrm{eff}}^{\mathrm{cit}}$[63]

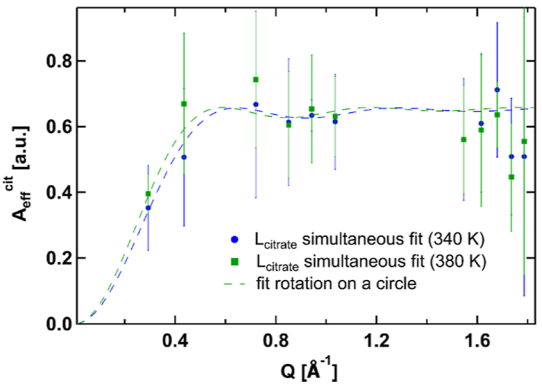

Figure 6. Amplitudes of the Lorentzian describing citrate motion fitted with continuous diffusion on a circle.

$$\mathrm{ISF}^{\mathrm{model}} = 1 - j_0^2(Qr) \tag{14}$$

where $j_0(x) = \frac{1}{x}\sin(x)$ is the spherical Bessel function of the zeroth order.

The model describes a ligand molecule attached with one end to the surface of an NP and rotating around an axis perpendicular to the surface. In this situation, each hydrogen atom would have its own circle of rotation. Therefore, there should be five Lorentzians, i.e., one for each hydrogen. Yet, we cannot resolve individual H atom motions and thus obtain an average radius of rotation of ∼5 Å. Besides, the ligand could have another rotational axis, e.g., around the backbone of the ligand chain.[25] Given the size of the error bars and the fact that only one reliable data point is available in the low Q range where the amplitude starts to approach zero, the interpretation of the geometry of citrate motion based on the corresponding ISF is not entirely definitive. A more detailed description of the ligand rotation would require an increased number of reliable data points, especially toward low Q values. Nevertheless, the Q dependence of $A_{\mathrm{eff}}^{\mathrm{cit}}$ in Figure 6 is consistent with rotational motion, and therefore, ligands are firmly grafted on the surface of the IONPs.

CONCLUSIONS

In this work, a comprehensive QENS investigation was conducted in the temperature range of 2 to 380 K to examine the diffusion dynamics of citrate ligands and water molecules on the surface of IONPs.

The FWS uncovered at least three distinct dynamical processes. Two of them are of a magnetic origin and start to be visible at around 50 K. One magnetic process is only apparent at the magnetic Bragg peak, while the other is present across all Q values. The obtained activation energy for the non-Bragg magnetic process is 20.8 ± 2.8 meV, in agreement with the previously obtained values for superparamagnetic relaxations of 19.8 meV.

The water and citrate motions were distinguished by comparing samples equilibrated in D_2O and H_2O. A simultaneous fit approach was implemented to create a coherent dynamical model. Elastic and inelastic FWSs, as well as ERS at two different temperatures (340 and 380 K), were fitted with shared parameters. Citrate molecules do not exhibit translational diffusion and likely undergo a localized rotational motion. It is characterized by a relaxation time limit of 0.21 ps and an activation energy of 240 meV. Water molecules diffuse translationally with a relaxation time limit of

https://doi.org/10.1021/acs.jpcc.4c00479
J. Phys. Chem. C 2024, 128, 11661−11671

0.12 ps and an activation energy of 190 meV. The diffusion coefficient of water at 360 K was estimated to be $\sim 9 \times 10^{-11}$ m^2/s.

Considering the complexity of the system, further investigations are required to investigate the magnetic relaxations and the dynamics of residual water molecules. The simultaneous fit approach, however, proves to be very useful for disentangling various dynamic components in complex systems such as magnetic NPs in contact with organic molecules and water.

■ ASSOCIATED CONTENT

Supporting Information

The Supporting Information is available free of charge at https://pubs.acs.org/doi/10.1021/acs.jpcc.4c00479.

Sample characterization, detector bank numbers and corresponding Q values, neutron powder diffraction, model equations, logarithmic-scale QENS plots, and magnetic relaxation (PDF)

■ AUTHOR INFORMATION

Corresponding Author

Mirijam Zobel − *JCNS-3: Neutron Analytics for Energy Research, Forschungszentrum Jülich GmbH, Wilhelm-Johnen-Straße, Jülich 52428, Germany; Institute of Crystallography, RWTH Aachen University, Aachen 52066, Germany;* orcid.org/0000-0002-8207-8316; Email: m.zobel@fz-juelich.de

Authors

Maksim S. Plekhanov − *Institute of Crystallography, RWTH Aachen University, Aachen 52066, Germany*

Sabrina L. J. Thomä − *Institute of Crystallography, RWTH Aachen University, Aachen 52066, Germany; Center for X-ray Analytics, Empa−Swiss Federal Laboratories for Materials, Science, and Technology, Dübendorf CH-8600, Switzerland;* orcid.org/0000-0002-1636-0508

Andreas Magerl − *Department of Physics, Friedrich-Alexander University, Biophysics Group, Erlangen 91052, Germany; JCNS-3: Neutron Analytics for Energy Research, Forschungszentrum Jülich GmbH, Wilhelm-Johnen-Straße, Jülich 52428, Germany*

Markus Appel − *Institut Laue-Langevin, Grenoble Cedex 9 38042, France*

Complete contact information is available at: https://pubs.acs.org/10.1021/acs.jpcc.4c00479

Author Contributions

M.Z. conceived and supervised the project. S.L.J.T. prepared all samples and performed complementary analytics (TGA and CHN). M.A., A.M., and M.Z. measured the samples. M.P. analyzed all data and wrote the first draft of the manuscript. A.M. contributed to the first round of data analysis and interpretation. M.Z. and A.M. were strongly involved in data analysis with M.P. The manuscript was jointly revised to the final form.

Notes

The authors declare no competing financial interest.

■ ACKNOWLEDGMENTS

We acknowledge funding by the Deutsche Forschungsgemeinschaft (DFG, German Research Foundation) via ZO 369/3-1, as well as RWTH Aachen University for the special commitment scholarship (STIBET I). We acknowledge beamtimes EASY-636, INTER-528, and 9-12-648 at IN16B (ILL) and beamtime ID 13387 at Emu (ANSTO). We thank the respective beamline scientists A. Klapproth (ANSTO) and N. De Souza (ANSTO) for assistance in operating the instruments. Furthermore, we acknowledge R. Zorn, JCNS-1, Forschungszentrum Jülich, for discussion, as well as B. Frick, ILL. We acknowledge support from M. Schwarzmann and A. Dietel for TGA and CHN analytics. We are grateful to M. Dulle, JCNS-1, Forschungszentrum Jülich, for SAXS measurements.

■ REFERENCES

(1) Roca, A. G.; Gutiérrez, L.; Gavilán, H.; Fortes Brollo, M. E.; Veintemillas-Verdaguer, S.; Morales, M.; del, P. Design Strategies for Shape-Controlled Magnetic Iron Oxide Nanoparticles. *Adv. Drug Delivery Rev.* **2019**, *138*, 68−104.

(2) Amstad, E.; Textor, M.; Reimhult, E. Stabilization and Functionalization of Iron Oxide Nanoparticles for Biomedical Applications. *Nanoscale* **2011**, *3* (7), 2819.

(3) Vangijzegem, T.; Stanicki, D.; Laurent, S. Magnetic Iron Oxide Nanoparticles for Drug Delivery: Applications and Characteristics. *Expert Opin. Drug Delivery* **2019**, *16* (1), 69−78.

(4) Oehlsen, O.; Cervantes-Ramírez, S. I.; Cervantes-Avilés, P.; Medina-Velo, I. A. Approaches on Ferrofluid Synthesis and Applications: Current Status and Future Perspectives. *ACS Omega* **2022**, *7* (4), 3134−3150.

(5) Saraswathy, A.; Nazeer, S. S.; Jeevan, M.; Nimi, N.; Arumugam, S.; Harikrishnan, V. S.; Varma, P. H.; Jayasree, R. S. Citrate Coated Iron Oxide Nanoparticles with Enhanced Relaxivity for in Vivo Magnetic Resonance Imaging of Liver Fibrosis. *Colloids Surf., B* **2014**, *117*, 216−224.

(6) Abo-zeid, Y.; Ismail, N. S. M.; McLean, G. R.; Hamdy, N. M. A Molecular Docking Study Repurposes FDA Approved Iron Oxide Nanoparticles to Treat and Control COVID-19 Infection. *Eur. J. Pharm. Sci.* **2020**, *153*, 105465.

(7) Le Goas, M.; Saber, J.; Bolívar, S. G.; Rabanel, J.-M.; Awogni, J.-M.; Boffito, D. C.; Banquy, X. (In)Stability of Ligands at the Surface of Inorganic Nanoparticles: A Forgotten Question in Nanomedicine? *Nano Today* **2022**, *45*, 101516.

(8) Wang, X.; Wang, X.; Bai, X.; Yan, L.; Liu, T.; Wang, M.; Song, Y.; Hu, G.; Gu, Z.; Miao, Q.; Chen, C. Nanoparticle Ligand Exchange and Its Effects at the Nanoparticle-Cell Membrane Interface. *Nano Lett.* **2019**, *19* (1), 8−18.

(9) Liu, M.; Ma, Y.; Wang, R. Y. Modifying Thermal Transport in Colloidal Nanocrystal Solids with Surface Chemistry. *ACS Nano* **2015**, *9* (12), 12079−12087.

(10) Bian, H.; Li, J.; Chen, H.; Yuan, K.; Wen, X.; Li, Y.; Sun, Z.; Zheng, J. Molecular Conformations and Dynamics on Surfaces of Gold Nanoparticles Probed with Multiple-Mode Multiple-Dimensional Infrared Spectroscopy. *J. Phys. Chem. C* **2012**, *116* (14), 7913−7924.

(11) Ionita, P.; Volkov, A.; Jeschke, G.; Chechik, V. Lateral Diffusion of Thiol Ligands on the Surface of Au Nanoparticles: An Electron Paramagnetic Resonance Study. *Anal. Chem.* **2008**, *80* (1), 95−106.

(12) Dulle, M.; Jaber, S.; Rosenfeldt, S.; Radulescu, A.; Förster, S.; Mulvaney, P.; Karg, M. Plasmonic Gold-Poly(N-Isopropylacrylamide) Core-Shell Colloids with Homogeneous Density Profiles: A Small Angle Scattering Study. *Phys. Chem. Chem. Phys.* **2015**, *17* (2), 1354−1367.

(13) Redel, E.; Walter, M.; Thomann, R.; Vollmer, C.; Hussein, L.; Scherer, H.; Krüger, M.; Janiak, C. Synthesis, Stabilization, Functionalization and, DFT Calculations of Gold Nanoparticles in Fluorous Phases (PTFE and Ionic Liquids). *Chem.—Eur. J.* **2009**, *15* (39), 10047−10059.

(14) Wu, Z.-P.; Shan, S.; Zang, S.-Q.; Zhong, C.-J. Dynamic Core-Shell and Alloy Structures of Multimetallic Nanomaterials and Their Catalytic Synergies. *Acc. Chem. Res.* **2020**, *53* (12), 2913−2924.
(15) Harris, R. A.; van der Walt, H.; Shumbula, P. M. Molecular Dynamics Study on Iron Oxide Nanoparticles Stabilised with Sebacic Acid and 1,10-Decanediol Surfactants. *J. Mol. Struct.* **2013**, *1048*, 18−26.
(16) Woehrle, G. H.; Brown, L. O.; Hutchison, J. E. Thiol-Functionalized, 1.5-Nm Gold Nanoparticles through Ligand Exchange Reactions: Scope and Mechanism of Ligand Exchange. *J. Am. Chem. Soc.* **2005**, *127* (7), 2172−2183.
(17) Price, W. S. Pulsed-Field Gradient Nuclear Magnetic Resonance as a Tool for Studying Translational Diffusion: Part 1. Basic Theory. *Concepts Magn. Reson.* **1997**, *9* (5), 299−336.
(18) Polito, L.; Colombo, M.; Monti, D.; Melato, S.; Caneva, E.; Prosperi, D. Resolving the Structure of Ligands Bound to the Surface of Superparamagnetic Iron Oxide Nanoparticles by High-Resolution Magic-Angle Spinning NMR Spectroscopy. *J. Am. Chem. Soc.* **2008**, *130* (38), 12712−12724.
(19) Hempelmann, R. *Quasielastic Neutron Scattering and Solid State Diffusion*; Oxford University Press: Oxford, 2000; ..
(20) Sears, V. F. Neutron Scattering Lengths and Cross Sections. *Neutron News* **1992**, *3* (3), 26−37.
(21) Marry, V.; Dubois, E.; Malikova, N.; Breu, J.; Haussler, W. Anisotropy of Water Dynamics in Clays: Insights from Molecular Simulations for Experimental QENS Analysis. *J. Phys. Chem. C* **2013**, *117* (29), 15106−15115.
(22) Paradossi, G.; Cavalieri, F.; Chiessi, E.; Telling, M. T. F. Supercooled Water in PVA Matrixes: I. An Incoherent Quasi-Elastic Neutron Scattering (QENS) Study. *J. Phys. Chem. B* **2003**, *107* (33), 8363−8371.
(23) Abe, H.; Takekiyo, T.; Yoshimura, Y.; Shimizu, A. Static and Dynamic Properties of Nano-Confined Water in Room-Temperature Ionic Liquids. *J. Mol. Liq.* **2019**, *290*, 111216.
(24) Mamontov, E.; Wesolowski, D. J.; Vlcek, L.; Cummings, P. T.; Rosenqvist, J.; Wang, W.; Cole, D. R. Dynamics of Hydration Water on Rutile Studied by Backscattering Neutron Spectroscopy and Molecular Dynamics Simulation. *J. Phys. Chem. C* **2008**, *112* (32), 12334−12341.
(25) Jansen, M.; Juranyi, F.; Yarema, O.; Seydel, T.; Wood, V. Ligand Dynamics in Nanocrystal Solids Studied with Quasi-Elastic Neutron Scattering. *ACS Nano* **2021**, *15* (12), 20517−20526.
(26) Seydel, T.; Koza, M. M.; Matsarskaia, O.; André, A.; Maiti, S.; Weber, M.; Schweins, R.; Prévost, S.; Schreiber, F.; Scheele, M. A Neutron Scattering Perspective on the Structure, Softness and Dynamics of the Ligand Shell of PbS Nanocrystals in Solution. *Chem. Sci.* **2020**, *11* (33), 8875−8884.
(27) Sharma, A.; Kruteva, M.; Zamponi, M.; Ehlert, S.; Richter, D.; Förster, S. Quasielastic Neutron Scattering Reveals the Temperature Dependent Rotational Dynamics of Densely Grafted Oleic Acid. *J. Chem. Phys.* **2022**, *156* (16), 164908.
(28) Sharma, A.; Kruteva, M.; Zamponi, M.; Ehlert, S.; Richter, D.; Förster, S. Influence of Molecular Weight on the Distribution of Segmental Relaxation in Polymer Grafted Nanoparticles. *Phys. Rev. Mater.* **2022**, *6* (1), L012601.
(29) Jhalaria, M.; Buenning, E.; Huang, Y.; Tyagi, M.; Zorn, R.; Zamponi, M.; García-Sakai, V.; Jestin, J.; Benicewicz, B. C.; Kumar, S. K. Accelerated Local Dynamics in Matrix-Free Polymer Grafted Nanoparticles. *Phys. Rev. Lett.* **2019**, *123*, 158003.
(30) Pradeep, T.; Mitra, S.; Nair, A. S.; Mukhopadhyay, R. Dynamics of Alkyl Chains in Monolayer-Protected Au and Ag Clusters and Silver Thiolates: A Comprehensive Quasielastic Neutron Scattering Investigation. *J. Phys. Chem. B* **2004**, *108* (22), 7012−7020.
(31) Bailey, E. J.; Winey, K. I. Dynamics of Polymer Segments, Polymer Chains, and Nanoparticles in Polymer Nanocomposite Melts: A Review. *Prog. Polym. Sci.* **2020**, *105*, 101242.
(32) Shrestha, S.; Jiang, P.; Sousa, M. H.; Morais, P. C.; Mao, Z.; Gao, C. Citrate-Capped Iron Oxide Nanoparticles Impair the Osteogenic Differentiation Potential of Rat Mesenchymal Stem Cells. *J. Mater. Chem. B* **2016**, *4* (2), 245−256.
(33) Milek, T.; Zahn, D. A Surfactants Walk to Work: Modes of Action of Citrate Controlling (10−10) and (000−1) Zinc Oxide Surface Growth from Solution. *Z. Anorg. Allg. Chem.* **2016**, *642* (16), 902−905.
(34) Klausen, S. N.; Lefmann, K.; Lindgård, P.-A.; Clausen, K. N.; Hansen, M. F.; Bødker, F.; Mørup, S.; Telling, M. An Inelastic Neutron Scattering Study of Hematite Nanoparticles. *J. Magn. Magn. Mater.* **2003**, *266* (1−2), 68−78.
(35) Gazeau, F.; Dubois, E.; Hennion, M.; Perzynski, R.; Raikher, Y. Quasi-Elastic Neutron Scattering on γ-Fe $_2$ O $_3$ Nanoparticles. *Europhys. Lett.* **1997**, *40* (5), 575−580.
(36) Eckardt, M.; Thomä, S. L. J.; Dulle, M.; Hörner, G.; Weber, B.; Förster, S.; Zobel, M. Long-Term Colloidally Stable Aqueous Dispersions of ≤ 5 Nm Spinel Ferrite Nanoparticles. *ChemistryOpen* **2020**, *9* (11), 1214−1220.
(37) Thomä, S. L. J.; Krauss, S. W.; Eckardt, M.; Chater, P.; Zobel, M. Atomic Insight into Hydration Shells around Facetted Nanoparticles. *Nat. Commun.* **2019**, *10* (1), 995.
(38) Zobel, M.; Appel, M. *Water Dynamics on Iron Oxide Nanoparticles*; Institut Laue-Langevin Database, 2020..
(39) Zobel, M.; Appel, M.; Feghelm, A.; Magerl, A.; Thomae, S. *Diffusion Dynamics of Water and Citrate Molecules on the Surface of Iron Oxide Nanoparticles*; Institut Laue-Langevin Database, 2021..
(40) Appel, M.; Frick, B.; Magerl, A. First Results with the Neutron Backscattering and TOF Spectrometer Option BATS on IN16B. *Phys. B: Condens. Matter* **2019**, *562*, 6−8.
(41) Zobel, M.; Appel, M.; Magerl, A.; Thomae, S. *Diffusion in the Liquid Interface Region of IONPs*; Institut Laue-Langevin Database, 2021..
(42) Arnold, O.; Bilheux, J. C.; Borreguero, J. M.; Buts, A.; Campbell, S. I.; Chapon, L.; Doucet, M.; Draper, N.; Ferraz Leal, R.; Gigg, M. A.; et al. Mantid—Data Analysis and Visualization Package for Neutron Scattering and SR Experiments. *Nucl. Instrum. Methods Phys. Res., Sect. A* **2014**, *764*, 156−166.
(43) Studer, A. J.; Hagen, M. E.; Noakes, T. J. Wombat: The High-Intensity Powder Diffractometer at the OPAL Reactor. *Phys. B: Condens. Matter* **2006**, *385*−*386*, 1013−1015.
(44) Toby, B. H.; Von Dreele, R. B. *GSAS-II*: the genesis of a modern open-source all purpose crystallography software package. *J. Appl. Crystallogr.* **2013**, *46* (2), 544−549.
(45) Perez-Mato, J. M.; Gallego, S. V.; Tasci, E. S.; Elcoro, L.; de la Flor, G.; Aroyo, M. I. Symmetry-Based Computational Tools for Magnetic Crystallography. *Annu. Rev. Mater. Res.* **2015**, *45* (1), 217−248.
(46) Sabrina, L. J. Thomä; Mirijam Zobel. Ethanol-Water Motifs - a Re-Interpretation of the Double-Difference Pair Distribution Functions of Aqueous Iron Oxide Nanoparticle Dispersions. *J. Chem. Phys.* **2024**, *158* (22), 224704.
(47) Petkov, V.; Cozzoli, P. D.; Buonsanti, R.; Cingolani, R.; Ren, Y. Size, Shape, and Internal Atomic Ordering of Nanocrystals by Atomic Pair Distribution Functions: A Comparative Study of γ-Fe_2O_3 Nanosized Spheres and Tetrapods. *J. Am. Chem. Soc.* **2009**, *131* (40), 14264−14266.
(48) Shmakov, A. N.; Kryukova, G. N.; Tsybulya, S. V.; Chuvilin, A. L.; Solovyeva, L. P. Vacancy Ordering in γ-Fe_2O_3: Synchrotron X-Ray Powder Diffraction and High-Resolution Electron Microscopy Studies. *J. Appl. Crystallogr.* **1995**, *28* (2), 141−145.
(49) Girardet, T.; Venturini, P.; Martinez, H.; Dupin, J.-C.; Cleymand, F.; Fleutot, S. Spinel Magnetic Iron Oxide Nanoparticles: Properties, Synthesis and Washing Methods. *Appl. Sci.* **2022**, *12* (16), 8127.
(50) Bixner, O.; Lassenberger, A.; Baurecht, D.; Reimhult, E. Complete Exchange of the Hydrophobic Dispersant Shell on Monodisperse Superparamagnetic Iron Oxide Nanoparticles. *Langmuir* **2015**, *31* (33), 9198−9204.
(51) Hill, A. H.; Jacobsen, H.; Stewart, J. R.; Jiao, F.; Jensen, N. P.; Holm, S. L.; Mutka, H.; Seydel, T.; Harrison, A.; Lefmann, K.

Magnetic Properties of Nano-Scale Hematite, α-Fe_2O_3, Studied by Time-of-Flight Inelastic Neutron Spectroscopy. *J. Chem. Phys.* **2014**, *140* (4), 044709.
(52) Brown, W. F. Thermal Fluctuations of a Single-Domain Particle. *Phys. Rev.* **1963**, *130* (5), 1677−1686.
(53) Situm, A.; Rahman, M. A.; Goldberg, S.; Al-Abadleh, H. A. Spectral Characterization and Surface Complexation Modeling of Low Molecular Weight Organics on Hematite Nanoparticles: Role of Electrolytes in the Binding Mechanism. *Environ. Sci. Nano* **2016**, *3* (4), 910−926.
(54) Yeasmin, S.; Singh, B.; Kookana, R. S.; Farrell, M.; Sparks, D. L.; Johnston, C. T. Influence of Mineral Characteristics on the Retention of Low Molecular Weight Organic Compounds: A Batch Sorption-Desorption and ATR-FTIR Study. *J. Colloid Interface Sci.* **2014**, *432*, 246−257.
(55) Assis, M. B. d. S.; Werneck, I. H. S. R.; de Moraes, G. N.; Semaan, F. S.; Pacheco Pereira, R. Citrate-Capped Iron Oxide Nanoparticles: Ultrasound-Assisted Synthesis, Structure and Thermal Properties. *Mater. Res. Express* **2019**, *6* (4), 045064.
(56) Mamontov, E.; Vlcek, L.; Wesolowski, D. J.; Cummings, P. T.; Wang, W.; Anovitz, L. M.; Rosenqvist, J.; Brown, C. M.; Garcia Sakai, V. Dynamics and Structure of Hydration Water on Rutile and Cassiterite Nanopowders Studied by Quasielastic Neutron Scattering and Molecular Dynamics Simulations. *J. Phys. Chem. C* **2007**, *111* (11), 4328−4341.
(57) Jørgensen, J. E.; Mosegaard, L.; Thomsen, L. E.; Jensen, T. R.; Hanson, J. C. Formation of γ-Fe_2O_3 Nanoparticles and Vacancy Ordering: An in Situ X-Ray Powder Diffraction Study. *J. Solid State Chem.* **2007**, *180* (1), 180−185.
(58) Köhler, T.; Feoktystov, A.; Petracic, O.; Kentzinger, E.; Bhatnagar-Schöffmann, T.; Feygenson, M.; Nandakumaran, N.; Landers, J.; Wende, H.; Cervellino, A.; et al. Mechanism of Magnetization Reduction in Iron Oxide Nanoparticles. *Nanoscale* **2021**, *13* (14), 6965−6976.
(59) Sinha, S. K.; Sirota, E. B.; Garoff, S.; Stanley, H. B. X-Ray and Neutron Scattering from Rough Surfaces. *Phys. Rev. B* **1988**, *38* (4), 2297−2311.
(60) Grapengeter, H. H.; Alefeld, B.; Kosfeld, R. An Investigation of Micro-Brownian Motions in Polydimethylsiloxane by Complementary Incoherent-Neutron-Scattering and Nuclear-Magnetic-Resonance Experiments below Room Temperature. *Colloid Polym. Sci.* **1987**, *265*, 226−233.
(61) Mamontov, E.; Smith, R. W.; Billings, J. J.; Ramirez-Cuesta, A. J. Simple Analytical Model for Fitting QENS Data from Liquids. *Phys. B: Condens. Matter* **2019**, *566*, 50−54.
(62) Krynicki, K.; Green, C. D.; Sawyer, D. W. Pressure and Temperature Dependence of Self-Diffusion in Water. *Faraday Discuss. Chem. Soc.* **1978**, *66*, 199.
(63) Bée, M. *Quasielastic Neutron Scattering*; Adam Hilger, 1988.

https://doi.org/10.1021/acs.jpcc.4c00479
J. Phys. Chem. C 2024, 128, 11661−11671